Original Research

Liver Lesion Conspicuity During Real-Time MR-Guided Radiofrequency Applicator Placement Using Spoiled Gradient Echo and Balanced Steady-State Free Precession Imaging

Hansjörg Rempp, MD,[1]* Henning Loh,[1] Rüdiger Hoffmann, MD,[1] Eva Rothgang, MS,[2] Li Pan, PhD,[3] Claus D. Claussen, MD,[1] and Stephan Clasen, MD[1]

Purpose: To retrospectively evaluate the conspicuity of liver lesions in a fluoroscopic spoiled gradient echo (GRE) and a balanced steady-state free precession (SSFP) magnetic resonance imaging (MRI) sequence.

Materials and Methods: In all, 103 patients with hepatocellular carcinomas (HCC) (41) or liver metastases (67) were treated using MR-guided radiofrequency ablation in a wide-bore 1.5 T scanner. A multislice real-time spoiled GRE sequence allowing for a T1 weighting (T1W) and a balanced SSFP sequence allowing for a T2/T1W contrast were used for MR guidance. The contrast-to-noise-ratio (CNR) of the lesions was calculated and lesion conspicuity was assessed retrospectively (easily detectable / difficult to detect / not detectable).

Results: HCC was easily detectable in 33/52% (GRE/SSFP), difficult to detect in 30/18%, and not detectable in 37/30% of the cases. Mean CNR varied widely (9.1 for GRE vs. 16.4 for SSFP). Liver metastases were easily detectable in 58/41% (GRE/SSFP), difficult to detect in 14/21%, and not detectable in 28/38% of the cases. Mean CNR for liver metastases was 11.5 (GRE) vs. 12.7 (SSFP). Twenty percent of all lesions could not be detected with either of the MR fluoroscopy sequences.

Conclusion: MR fluoroscopy using GRE and SSFP contrast enabled real-time detectability of 80% of the liver lesions.

Key Words: MR-guided intervention; MR fluoroscopy; radiofrequency ablation; steady-state free precession sequence; real-time MR sequences; interventional MRI

MINIMALLY INVASIVE TUMOR THERAPIES for liver lesions have gained increased importance during the last decade (1–5). Radiofrequency (RF) ablation or other local ablation therapies are the recommended approach for early stage hepatocellular carcinoma (HCC) according to the Barcelona Clinic Liver Cancer (BCLC) staging classification and the American Association of the Study of Liver Diseases (AASLD) (6,7). Thermal ablations are also the first choice of treatment for unresectable isolated hepatic metastases. Image guidance plays a key role in accurate applicator placement and in ensuring a targeted, safe, and complete treatment.

Ultrasound and computed tomography (CT) are the most widespread imaging modalities for percutaneous device placement. Ultrasound is inexpensive and widely available; however, lesion conspicuity can be limited and the generation of gas bubbles further decreases visibility during ablation (8,9). CT precisely demonstrates the position of the applicators; however, the differentiation between the ablation zone and residual tumor tissue is often difficult without administration of contrast agent (10,11).

Restricted patient access, availability, and cost have limited the use of magnetic resonance imaging (MRI) for thermal ablation guidance. However, the high soft-tissue contrast provides excellent tumor and ablation zone visualization, while avoiding radiation exposure to the patient and interventionalist. MR thermometry further supports enhanced therapy monitoring (12). T1-weighted spoiled gradient echo (GRE) and T2/T1-weighted balanced steady-state free precession (SSFP) imaging can be used in an interactive, real-time mode to allow free selection of imaging planes to ensure continuous visualization of the target lesion, surrounding structures, and the RF applicator. This study retrospectively evaluates the conspicuity of liver

Figure 1. a: Size of the HCC lesions treated. **b:** Size of the liver metastases treated. [Color figure can be viewed in the online issue, which is available at wileyonlinelibrary.com.]

lesions in a fluoroscopic spoiled GRE and a balanced SSFP MR sequence used in the context of MR-guided RF ablation procedures.

MATERIALS AND METHODS
Patients and Treated Tumors

Between 2009 and 2011, 103 patients with 108 liver tumors were treated using RF ablation in our hospital. All hepatic RF ablations were performed under MR guidance.

Forty-one patients (8 women and 33 men) were treated for HCC. Forty-one HCCs were treated; mean lesion size was 22 mm (range: 10–44 mm; standard deviation [SD] 8 mm) (Fig. 1a). The patients were between 27 and 83 years old and the mean patient age was 68 years. HCC diagnosis was based on the EASL criteria or on a biopsy of the lesion (13,14).

Sixty-two patients (27 women and 35 men) suffered from liver metastases. The patients were between 25 and 85 years old, mean patient age 61 years. A total number of 67 metastases were treated, among them 35 from colorectal carcinoma. Ten other lesions were metastases of a resected cholangiocellular carcinoma, eight patients had breast cancer, seven presented with metastatic melanoma, three with sarcoma, two with ovarian cancer, and one patient each with metastasis of a neuroendocrine carcinoma and an esophageal cancer. Mean lesion size was 20 mm (range: 7–55 mm; SD 10 mm) (Fig. 1b).

An interdisciplinary tumor board approved the indication for MR-guided RF ablation in all patients. All patients signed informed consent to the procedure at least 1 day before the intervention. The study was approved by the Institutional Review Board. Patients were excluded from the study if a contrast agent was administered directly before the intervention.

Procedure and MR Sequences

All patients were treated inside a wide-bore 1.5 T MR scanner (MAGNETOM Espree, Siemens Healthcare, Erlangen, Germany). All steps of the intervention were performed inside the bore. The patients were placed feet forward in a supine or oblique position. The intervention began with a short planning step using T1- and T2-weighted sequences (Table 1). An orientation grid (Daum, Schwerin, Germany) or a capsule was used to mark the puncture site. Skin was disinfected and local anesthesia was injected to the puncture site. For signal reception, 6 elements of the spine phased array coil were combined with a 6-element body phased array coil placed over the liver and an additional 1-element loop coil placed directly around the puncture site. The intervention was performed

Table 1
MR Pulse Sequence Parameters

Sequence	TE (msec)	TR (msec)	Slice thickness (mm)	Matrix	Flip angle	Bandwidth (Hz/pixel)
Diagnostic MR sequences (selected)						
HASTE	116	1100	6	205 x 256	120	490
T1 VIBE	1.05	2.95	2.3	146 x 256	10	558
T1 spoiled GRE	4.14	212	6	256 x 256	70	140
T2 TSE	101	4185	6	80 x 320	150	260
Fluoroscopic imaging using BEAT_IRTTT						
T1 spoiled GRE	1.98	3.33	5	128 x 128	15	420
T2/T1 balanced SSFP	2.24	4.48	5	128 x 128	50	300

HASTE, half acquisition single shot turbo spin echo (TSE) sequence; TSE, turbo spin echo sequence (breath-hold technique); VIBE, volumetric interpolated breathhold examination (a T1-weighted fast 3D spoiled gradient echo sequence), BEAT_IRTTT (multiplanar interactive real-time sequence, Siemens Corporate Technology, Baltimore, MD).

under analgesic sedation using Piritramide and Diazepam (95 patients) or under general anesthesia (eight patients). Depending on lesion size, one to four 16G MR-compatible RF applicators (Celon, Teltow, Germany) were placed under continuous real-time image guidance into the lesion. The length of the 16G applicators ranged from 10–20 cm, and the active tip measured 2–4 cm in length.

A fluoroscopic multislice sequence with image contrast flexibility was used for applicator placement (BEAT_IRTTT, work in progress, Siemens Corporate Technology, Baltimore, MD). The sequence allows switching between a T1-weighted image contrast using a spoiled gradient echo (GRE) sequence and a T2/T1-weighted image contrast using a balanced steady-state free precession (SSFP) sequence, which is not a pure T2 image weighting (15).

Three image planes were continuously acquired and displayed during applicator placement. Two of the image planes were placed orthogonal to each other containing the applicator (transversal oblique and sagittal oblique). A third plane was placed close to the lesion in a plane crossing the other two image planes. The slice angulations could be changed interactively during the measurements if corrections were necessary. Table 1 describes the GRE and SSFP imaging parameters. The three slices were consecutively updated at rates of 426 msec and 580 msec,

respectively. This equates to single slice update rates every 1278 msec and 1740 msec, respectively.

Due to the retrospective nature of this study, some cases did not involve the use of both interactive, real-time GRE and SSFP imaging. The lesion may have been visible using the first sequence employed during that study, therefore usage of the second sequence was not needed. Further details are given in the results and are shown in Fig. 2. If the lesions were not visible in either of the image sequences, anatomic landmarks such as vessel bifurcations were used for orientation and a stepwise placement was performed with intermittent T1-weighted turbo spin echo (TSE) imaging.

Data Assessment

Visual Assessment

Lesion conspicuity was assessed by two independent readers (one interventional radiologist with 6 years of experience, H.R., and one noninterventional physician in training with 2 years of experience, H.L.). As ablation-induced coagulation necrosis changes the signal characteristics of tissue, only fluoroscopic images acquired before the first ablation cycle were evaluated. The lesion diameters in diagnostic preinterventional transversal T1-weighted spoiled GRE
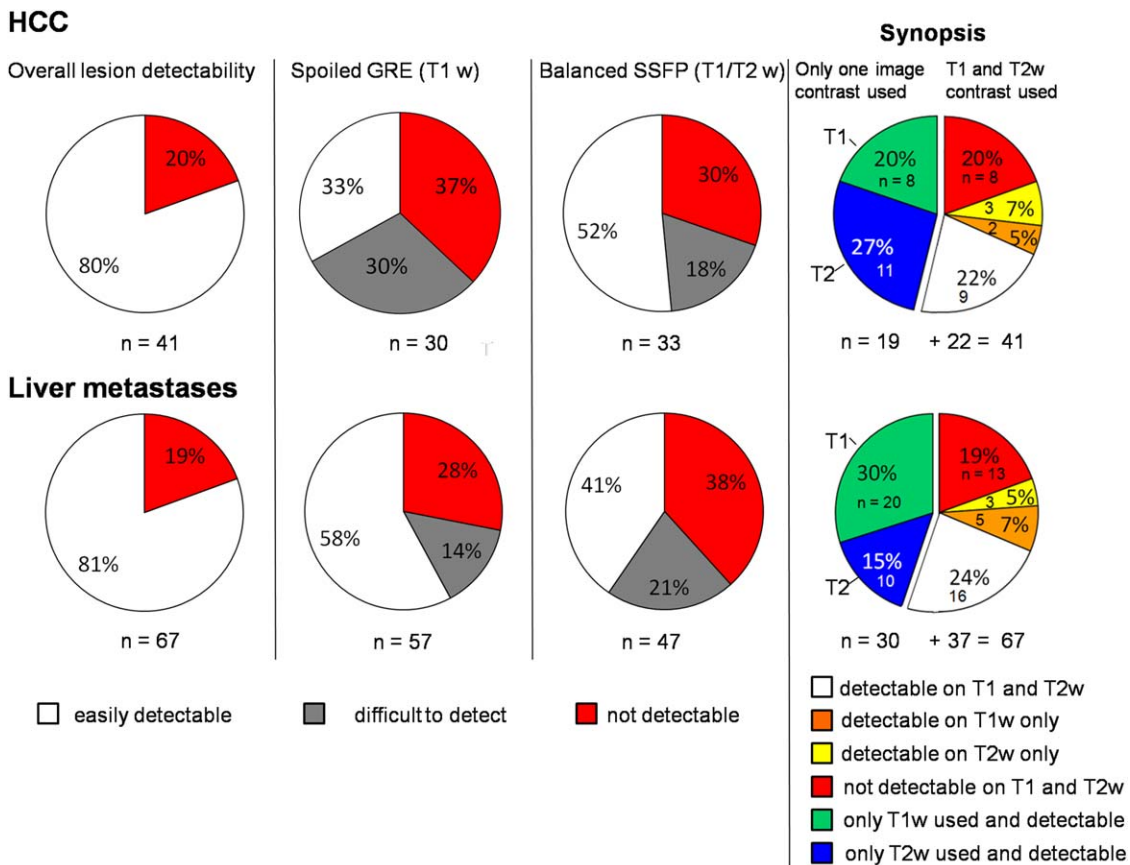
Figure 2. Results of visual lesion conspicuity assessment. Please note that not all lesions were imaged using both imaging contrasts; the total number of analyzed lesions is indicated below each graph. "Detectable" in the synopsis refers to lesions that were either classified as "easily detectable" or "difficult to detect." In case of nondetectable lesions, both the spoiled GRE and the balanced SSFP image contrast were used.
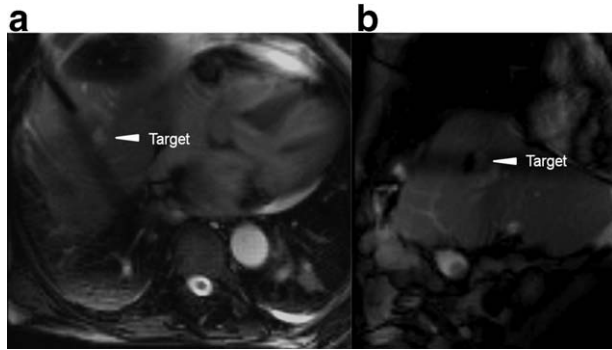
Figure 3. Balanced SSFP fluoroscopic imaging of an 82-year-old male patient with a 27-mm HCC in liver segment VIII. **a:** balanced SSFP fluoroscopic semi-transversal slice with the applicator approaching the lesion. **b:** Orthogonal slice at a later moment, when the applicator had reached the lesion at its lateral periphery. A second applicator is placed at the medial edge of the lesion. The lesion was classified with easily detectable.

images and T2-weighted TSE images (Table 1) were measured and compared to the lesion diameters in transverse or transverse oblique fluoroscopic images. If the lesion was smaller in the transverse fluoroscopic image, one of the other fluoroscopic image planes was selected in order to avoid partial volume effect. To account for potential movement of the tumor out of the imaging plane, all fluoroscopic images were reviewed and the one with the best tumor visualization was saved and used for formal evaluation.

The two readers independently classified the lesions as either (a) easily detectable, (b) difficult to detect, or (3) not detectable. Final lesions classifications were defined as follows: easily detectable (a) if both reviewers agreed, and not detectable (c), if classified so by at least one reader. All other lesions were classified as difficult to detect (b).

Contrast-to-Noise Ratio

The images selected to visually assess lesion conspicuity were also used for contrast-to-noise ratio (CNR) evaluation. A circular region of interest (ROI) adapted to the size of the lesion was placed on the target lesion and mean signal intensity was measured. The same
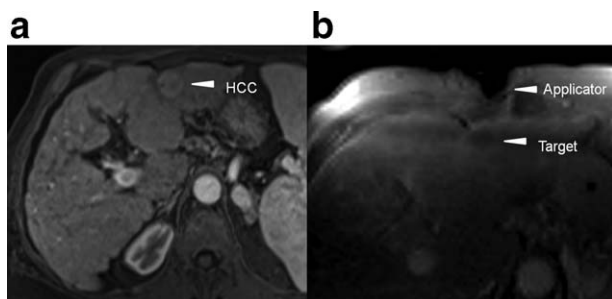
ROI was placed on a neighboring healthy area of the liver. We avoided measurements within saturation bands created by other imaging planes. Additionally, the CNR of the applicator and of large intrahepatic vessels was assessed using ROIs adapted to the size of the applicator artifact or the vessel. The CNR was calculated as the difference of the mean signal intensity in the liver ROI from the lesion/applicator/vessel ROI divided by the standard deviation of the noise represented by an ROI placed outside the body. Mean CNR of all lesions was calculated based on absolute CNR values.
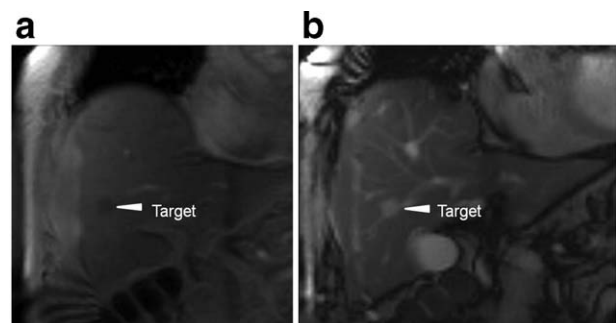
The CNR of the lesions in diagnostic imaging was assessed using the nonenhanced transversal preinterventional T1-weighted spoiled GRE and T2-weighted TSE images (Table 1).

RESULTS

HCC

Thirty-three of 41 lesions (80%) were easily detected using at least one of the two MR fluoroscopy sequences. For 14 out of these 33 lesions, both GRE and SSFP imaging was used. Eight lesions (8/41, 20%) with a mean size of 20 mm (range 10–33 mm), although imaged with both sequences, could not be detected using MR fluoroscopy. An overview of the visual assessment results is given in Fig. 2.

Thirty lesions were scanned using fluoroscopic GRE imaging; 33% of these lesions were easily detectable, 30% difficult to detect, and 37% not detectable. Thirty-three lesions were scanned using fluoroscopic balanced SSFP imaging; 52% of these lesions were easily detectable, 18% difficult to detect, and 30% not detectable. Thus, in balanced SSFP fluoroscopy more HCC lesions were easily detectable than in spoiled GRE fluoroscopy. The mean size of the lesions which could not be detected in spoiled GRE imaging was 21 mm vs. 20 mm in balanced SSFP imaging. Among the 11 HCC not detectable lesions in spoiled GRE imaging, eight were classified so by reader A and B, two by reader A, and one by reader B. Among the 10 HCC not detectable lesions balanced SSFP imaging, eight were classified so by reader A and B, one by reader A,

Figure 4. A 72-year-old female patient with a 23-mm HCC in the left liver lobe. **a:** Contrast-enhanced diagnostic imaging (preacquired before the study). **b:** Spoiled GRE fluoroscopic imaging. The lesion was classified as difficult to detect.

Figure 5. A 67-year-old male patient with an 18-mm colorectal cancer liver metastasis in liver segment V. The lesion can be easily detected in the (**a**) spoiled GRE and (**b**) balanced SSFP fluoroscopic imaging. The applicator is not displayed here. The metastasis was classified as easily detectable in both image contrasts.
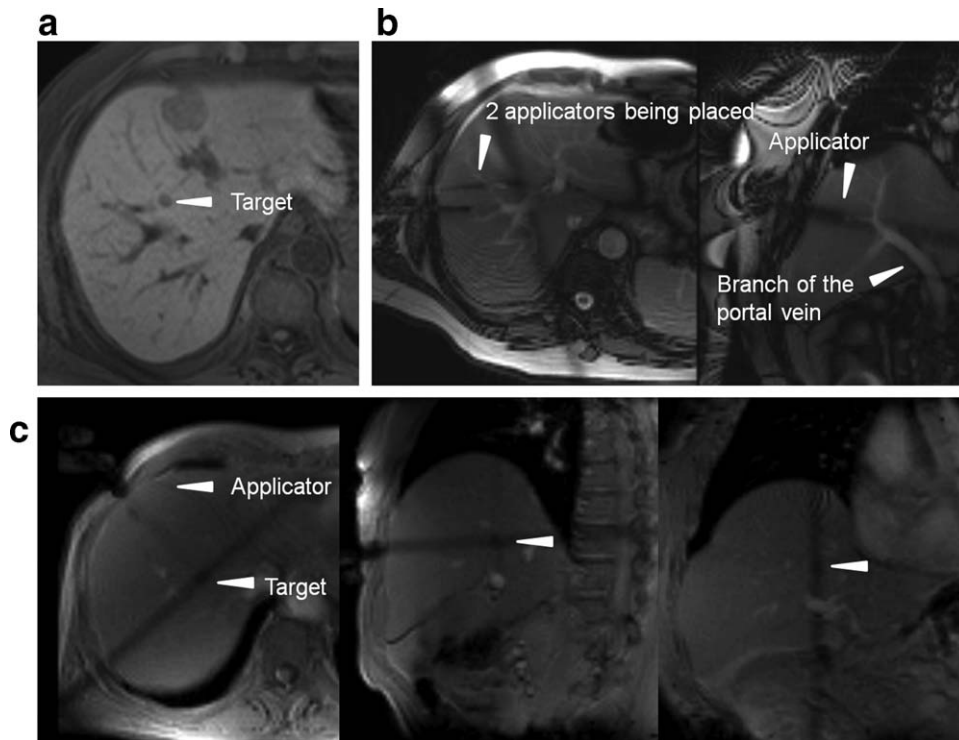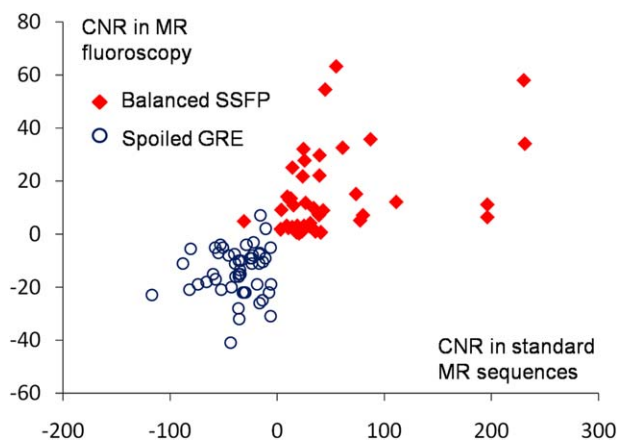
Figure 6. A 75-year-old male patient with 15-mm colon cancer liver metastases in segment VIII. **a:** T1-weighted pre-interventional imaging. Another metastasis in liver segment IVa will be treated by atypical resection. **b:** In order to visualize adjacent branches of the portal vein, balanced SSFP fluoroscopic imaging was chosen. The lesion was classified as not detectable in these images. **c:** When image contrast was changed to T1-weighted spoiled GRE, the lesion could be detected (positioned on the saturation bands of intersecting imaging slices for targeting).

and one by reader B. Examples of spoiled GRE and balanced SSFP fluoroscopic images are given in Figs. 3 and 4.

Liver Metastases

Thirteen of 67 liver metastases were not detectable in either of the tested contrast weightings (19%), while all other liver metastases were detectable in at least one of the image weightings (81%). Fifty-seven liver metastases were scanned using spoiled GRE fluoroscopic imaging; 58% of these lesions were easily detectable, 14% difficult to detect, and 28% not

Figure 7. CNR of the liver metastases as a function of the CNR in diagnostic MR sequences (T1-weighted spoiled GRE and T2-weighted TSE diagnostic sequences vs. T1-weighted spoiled GRE and predominantly T2-weighted balanced SSFP real-time sequences). Overall linear correlation is $r^2 = 0.46$. [Color figure can be viewed in the online issue, which is available at wileyonlinelibrary.com.]

detectable. Forty-seven liver metastases were scanned using balanced SSFP fluoroscopic imaging; 41% of these metastases were easily detectable, 21% difficult to detect, and 38% not detectable. Thus, in spoiled GRE fluoroscopy more liver metastases were easily detectable than in balanced SSFP fluoroscopy. The mean size of the not detectable metastases using spoiled GRE and balanced SSFP fluoroscopy was 15 mm and 19 mm, respectively. Among the 16 not detectable metastases in spoiled GRE imaging, 14 were classified so by both readers and two only by reader A. In balanced SSFP imaging, 12 of the 18 lesions were classified as not detectable by both readers, two by reader A and four by reader B. Examples of liver metastases in fluoroscopy are given in Figs. 5 and 6.

CNR in Standard Sequences and in Fluoroscopy

For both lesion types, highly variable CNR was observed in both diagnostic and fluoroscopic sequences using both contrasts. In all cases, the absolute value of CNR was higher in the diagnostic sequences than in MR fluoroscopy.

The majority of HCC were hypointense compared to the liver parenchyma in T1-weighted imaging. The mean absolute CNR of HCC in the nonenhanced T1-weighted GRE images was 24.6 (range: −106 to 62; median −15) vs. 9.1 (range: −30 to 10; median −9) in fluoroscopic spoiled GRE imaging. Two lesions were hyperintense compared to the liver parenchyma in diagnostic and fluoroscopic images showing a CNR of 3 and 10, respectively. It is anticipated that this is due to hemorrhage. In T2-weighted turbo spin echo images, the majority of lesions was hyperintense compared to the liver parenchyma. Mean CNR of HCC was

Table 2
Mean CNR and Lesion Size Depending on Visual Classification

| Lesion type	Contrast weighting	Visual classification	Number of lesions	Lesion size [mm]	Mean CNR in fluoroscopy	Mean CNR in diagnostic imaging
HCC	Spoiled GRE	Easily detectable	10	22.5 (10, 44)	17.3 (−30, 10)	39.4 (−106, 62)
		Difficult to detect	9	23.8 (10, 42)	8.4 (−19, 7)	26.1 (−73, 7)
		Not detectable	11	21.1 (12, 33)	not applicable	14.8 (−19, 7)
	Balanced SSFP	Easily detectable	17	24.2 (13, 44)	24.9 (6, 89)	41.5 (−3, 71)
		Difficult to detect	6	21.1 (15, 25)	10.0 (−6, 18)	30.9 (−32, 92)
		Not detectable	10	20.1 (10, 28)	not applicable	5.8 (3, 26)
Mets	Spoiled GRE	Easily detectable	33	20.5 (7, 52)	18.1 (−41, 14)	51.6.0 (−117, 70)
		Difficult to detect	8	23.7 (10, 48)	11.4 (−3, −25)	36.6 (−66, −14)
		Not detectable	16	15.1 (8, 23)	not applicable	22.9 (−38, −7)
	Balanced SSFP	Easily detectable	19	20.2 (14, 48)	24.0 (5, 63)	72.9 (12, 231)
		Difficult to detect	10	23.1 (10, 48)	13.4 (−4, 25)	54.3 (−31, 196)
		Not detectable	18	17.6 (8, 55)	not applicable	18.5 (3, 41)

HCC, hepatocellular carcinoma; Mets, liver metastases including metastases of cholangiocellular carcinoma. Minimal and maximal values are given in parentheses. Mean CNR is given as an absolute value.

25.5 (range: −32 to 92; median 16) in TSE vs. 16.4 (range: −6 to 89; median 11) in balanced SSFP fluoroscopy. A direct linear correlation between CNR in diagnostic imaging and fluoroscopic imaging could not be demonstrated (linear regression $r^2 = 0.21$).

The mean CNR of the liver metastases in nonenhanced T1-weighted GRE images was 37.1 (range: −117 to 70; median −36) vs. 11.5 (range: −41 to 14; median −10) in the fluoroscopic spoiled GRE imaging. Two of the metastatic melanomas were T1 hyperintense compared to the liver parenchyma; all other lesions were T1 hypointense to a variable extent. The mean CNR of the liver metastases in the T2-weighted TSE images was 43.3 (range: −31 to 231; median 27) vs. 12.7 (range: −4 to 63; median 9) in balanced SSFP fluoroscopy. The relation between the CNR of the metastases in diagnostic and fluoroscopic imaging is shown in Fig. 7.

The mean CNR values in diagnostic and fluoroscopic imaging were larger in the easily detectable group than in the other groups. Further information on the CNR values of lesions rated accordingly to the visual assessment is given in Table 2.

There was no strong correlation between lesion size and CNR. CNR of all lesions is shown as a function of lesion size in Fig. 8. The coefficient of determination
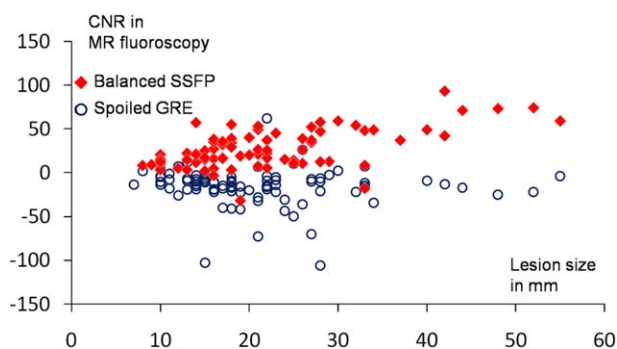
Figure 8. CNR of all lesions in spoiled GRE and balanced SSFP fluoroscopy as a function of lesion size. [Color figure can be viewed in the online issue, which is available at wileyonlinelibrary.com.]

in a linear regression was $r^2 = 0.06$ and 0.35 for spoiled GRE and balanced SSFP fluoroscopic imaging, respectively.

Applicators

The applicators were well visualized in both contrast weightings. The mean width of the applicator artifact was 7 ± 1 mm (mean ± SD) for the spoiled GRE sequence and 6 ± 1 mm for the balanced SSFP sequence. There was no blooming artifact at the tip of the applicator in either contrast weighting. Mean CNR of the applicator was 42.3 ± 10 for the spoiled GRE fluoroscopy and 26.2 ± 8 for the balanced SSFP sequence.

Vessels

Vessel visualization was better in balanced SSFP images. Mean CNR of large intrahepatic vessels was 18 ± 7 for spoiled GRE vs. 103 ± 17 for the balanced SSFP sequence.

DISCUSSION

Performing tumor ablation under MR guidance requires justification in an era of limited resources. Tumor ablation must compete with surgery and other therapeutic approaches in terms of safety and especially long-term therapy efficacy (16). The primary strength of MR is its high soft-tissue contrast and excellent visualization of even small lesions. This is of great importance for accurate applicator placement into the target lesion. In addition, MR allows one to continuously monitor the ablation progress as coagulated tissue can be well differentiated from untreated tumor tissue and healthy liver parenchyma (17). Additional tools, such as MR temperature mapping, might further improve patient safety and treatment efficacy (18).

The multiplanar imaging capabilities of MR are another strong argument for MR-guided thermal ablations. The use of wide-bore 1.5 T MR scanners allows

positioning the thermal applicator under continuous real-time imaging with the patient placed inside the bore (19–21). Special pulse sequences must be used for applicator placement, achieving both sufficient temporal and spatial resolution. These sequences evolved with the advances in the rapid generation of image contrast (22). Fast spin echo sequences, such as HASTE (half Fourier acquisition single shot turbo spin echo) sequences are strictly T2-weighted. Partial Fourier technique allows for an acquisition time of about 1000 msec per slice (23). From the gradient echo family, fast low angle shot (FLASH) sequences are favorable for targeting, as they provide a variety of image contrast (24). SSFP sequences also belong to the gradient echo family and are advantageous since blood and vessels appear bright on the images (15). The imaging contrast is determined by the T2* and T1 relaxation time of the tissue and can be modified by selecting the bandwidth, TR, TE, and flip angle, which allows for the generation of a T1 and T2-like image weighting (25). Despite a loss in CNR towards diagnostic MR sequences, image quality in balanced SSFP sequences is sufficient for clinical applications such as MR-guided biopsies (19,26). The combination of a predominantly T2-weighted balanced SSFP sequence and a T1-weighted spoiled GRE sequence was implemented to increase the imaging capabilities and to optimize the workflow during fluoroscopy.

Lesion visualization is a key component of MR fluoroscopy during applicator placement. We found lesion conspicuity was less dependent on lesion size than on CNR. This was determined through the visual assessment as well as by the CNR analysis, where values varied highly, not only reflecting different locations in the liver but also different initial imaging characteristics of the lesions. However, lesions with a diameter below the slice thickness of the fluoroscopic sequence are less detectable, since they are affected by the partial volume effect.

The ability to choose from two different contrast weightings in MR fluoroscopy offers various advantages. Most important, a number of lesions could only be visualized by one of the sequences. Due to the retrospective nature of the study, it is difficult to estimate the absolute number of these lesions; based on the cases where both were used, about a fifth of all lesions could only be visualized by one of the two image weightings. Furthermore, lesion conspicuity could be improved in a number of cases by using a T1- or a T2-like image contrast. For the majority of HCC lesions, the balanced SSFP images seemed to be more adequate; the majority of metastases could be better detected in spoiled GRE images, based on the visual assessment. The possibility of switching the image contrast also has practical advantages. In some cases, the display of vessels, cysts, or of a segmental cholestasis in the predominantly T2-weighted balanced SSFP images helps to ensure they are not hit by the applicator. If the structure in question has been passed, the contrast can be changed to a spoiled GRE, which better visualizes the moving applicator. Combined with the possibility of interactively adjusting the image planes during image acquisition it allows for an efficient workflow as an interruption of the fluoroscopy for an additional diagnostic sequence can be avoided.

However, regardless of the lesion type, one-fifth of the lesions could not be detected in either of the tested contrast weightings. These lesions fall in the group with the lowest CNR in nonenhanced diagnostic MRI. Different strategies for precise targeting in these cases can be used. Contrast agents can be used and targeting can be done during enhancement. However, lesion conspicuity may rapidly decrease after the administration of a contrast agent. Liver-specific contrast agents may be used alternatively in these cases (27,28). Superparamagnetic iron-oxide particles enable the visualization of lesions smaller than 1 cm over a longer period of time (29). Furthermore, alternative pulse sequences such as the more heavily T2-weighted HASTE sequence could improve the conspicuity of some lesions. In the cases presented here, a stepwise approach was used if the lesion could not be visualized in one of the available contrasts. MR fluoroscopy was interrupted for a diagnostic MR sequence in order to monitor the position of the probe in relation to the lesion. Anatomic landmarks, such as vessel bifurcations within the liver, were used to improve orientation. The intersecting saturation bands of the image planes were also used to improve the accuracy of the applicator orientation; however, care must be taken with regard to breathing movements causing a displacement of those lines.

Different limitations of this retrospective analysis must be mentioned. The data were collected in a mixed group of lesions with respect to lesion size and tumor entities. Clustering effects may play a role in our lesion-based analysis, as five patients with two lesions were included. The images for CNR assessment were carefully selected; however, errors might have occurred due to image planes which were not exactly centered at the lesions. The lesion location within the liver and its distance to the 6-element phased array coil which influence the signal intensities were not taken into account. The visual assessment of lesions is subjective and classification into three different groups is reader-dependent and results in rough categories. Not all lesions were imaged with both tested imaging contrasts.

In conclusion, the tested real-time spoiled GRE and balanced SSFP sequences allow for increased detectability of lesions and for improved lesion conspicuity due to the capability to adapt the contrast weighting. Metastases tend to be better visualized in spoiled GRE imaging, and HCC in balanced SSFP imaging. Lesion visualization seems to depend more on CNR in diagnostic T1- and T2-weighted images than on lesion size.

ACKNOWLEDGMENTS

REFERENCES

1. Lencioni R, Cioni D, Crocetti L, et al. Early-stage hepatocellular carcinoma in patients with cirrhosis: long-term results of percutaneous image-guided radiofrequency ablation. Radiology 2005; 234:961–967.
2. Gillams AR, Lees WR. Five-year survival in 309 patients with colorectal liver metastases treated with radiofrequency ablation. Eur Radiol 2009;19:1206–1213.
3. Goldberg SN, Ahmed M. Minimally invasive image-guided therapies for hepatocellular carcinoma. J Clin Gastroenterol 2002;35: S115–129.
4. Solbiati L, Livraghi T, Goldberg SN, et al. Percutaneous radiofrequency ablation of hepatic metastases from colorectal cancer: long-term results in 117 patients. Radiology 2001;221: 159–166.
5. Gervais DA, Arellano RS. Percutaneous tumor ablation for hepatocellular carcinoma. AJR Am J Roentgenol 2011;197:789–794.
6. Llovet JM. Updated treatment approach to hepatocellular carcinoma. J Gastroenterol 2005;40:225–235.
7. Bruix J, Sherman M. Management of hepatocellular carcinoma. Hepatology 2005;42:1208–1236.
8. Mulier S, Ni Y, Jamart J, Ruers T, Marchal G, Michel L. Local recurrence after hepatic radiofrequency coagulation: multivariate meta-analysis and review of contributing factors. Ann Surg 2005; 242:158–171.
9. Leyendecker JR, Dodd GD 3rd, Halff GA, et al. Sonographically observed echogenic response during intraoperative radiofrequency ablation of cirrhotic livers: pathologic correlation. AJR Am J Roentgenol 2002;178:1147–1151.
10. Goldberg SN, Gazelle GS, Compton CC, Mueller PR, Tanabe KK. Treatment of intrahepatic malignancy with radiofrequency ablation: radiologic-pathologic correlation. Cancer 2000;88:2452–2463.
11. Nghiem HV, Francis IR, Fontana R, et al. Computed tomography appearances of hypervascular hepatic tumors after percutaneous radiofrequency ablation therapy. Curr Probl Diagn Radiol 2002; 31:105–111.
12. Seror O, Lepetit-Coiffe M, Le Bail B, et al. Real time monitoring of radiofrequency ablation based on MR thermometry and thermal dose in the pig liver in vivo. Eur Radiol 2008;18:408–416.
13. EASL-EORTC clinical practice guidelines: management of hepatocellular carcinoma. J Hepatol 2012;56:908–943.
14. Bruix J, Sherman M. Management of hepatocellular carcinoma: an update. Hepatology 2011;53:1020–1022.
15. Duerk JL, Lewin JS, Wendt M, Petersilge C. Remember true FISP? A high SNR, near 1-second imaging method for T2-like contrast in interventional MRI at .2 T. J Magn Reson Imaging 1998; 8:203–208.
16. Mulier S, Ni Y, Jamart J, Michel L, Marchal G, Ruers T. Radiofrequency ablation versus resection for resectable colorectal liver metastases: time for a randomized trial? Ann Surg Oncol 2008; 15:144–157.
17. Rempp H, Waibel L, Hoffmann R, Claussen CD, Pereira PL, Clasen S. MR-guided radiofrequency ablation using a wide-bore 1.5-T MR system: clinical results of 213 treated liver lesions. Eur Radiol 2012;22:1972–1982.
18. Kickhefel A, Rosenberg C, Weiss CR, et al. Clinical evaluation of MR temperature monitoring of laser-induced thermotherapy in human liver using the proton-resonance-frequency method and predictive models of cell death. J Magn Reson Imaging 2011;33: 704–712.
19. Stattaus J, Maderwald S, Forsting M, Barkhausen J, Ladd ME. MR-guided core biopsy with MR fluoroscopy using a short, wide-bore 1.5-Tesla scanner: feasibility and initial results. J Magn Reson Imaging 2008;27:1181–1187.
20. Stattaus J, Maderwald S, Baba HA, et al. MR-guided liver biopsy within a short, wide-bore 1.5 Tesla MR system. Eur Radiol 2008; 18:2865–2873.
21. Richard HM 3rd, McMillan A, Staats PN, d'Othee BJ. Real-time MR imaging guidance for percutaneous core biopsy of US- and CT-negative lesion. J Vasc Interv Radiol 2012;23:1539–1542.
22. Yutzy SR, Duerk JL. Pulse sequences and system interfaces for interventional and real-time MRI. J Magn Reson Imaging 2008; 27:267–275.
23. Zimmermann H, Muller S, Gutmann B, et al. Targeted-HASTE imaging with automated device tracking for MR-guided needle interventions in closed-bore MR systems. Magn Reson Med 2006; 56:481–488.
24. Hasse A, Frahm J, Matthaei D, Hanicke W, Merbolt K-D. FLASH imaging. Rapid NMR imaging using low flip-angle pulses. J Magn Reson 1986;67:258–266.
25. Numminen K, Halavaara J, Isoniemi H, et al. Magnetic resonance imaging of the liver: true fast imaging with steady state free precession sequence facilitates rapid and reliable distinction between hepatic hemangiomas and liver malignancies. J Comput Assist Tomogr 2003;27:571–576.
26. Shimada K, Isoda H, Okada T, et al. Non-contrast-enhanced MR portography with time-spatial labeling inversion pulses: comparison of imaging with three-dimensional half-Fourier fast spin-echo and true steady-state free-precession sequences. J Magn Reson Imaging 2009;29:1140–1146.
27. Konig CW, Trubenbach J, Fritz J, Lauer UM, Claussen CD, Pereira PL. Contrast enhanced MR-guided biopsy of hepatocellular carcinoma. Abdom Imaging 2004;29:71–76.
28. Joarder R, de Jode M, Lamb GA, Gedroyc WM. The value of MnDPDP enhancement during MR guided laser interstitial thermoablation of liver tumors. J Magn Reson Imaging 2001;13:37–41.
29. Kim MJ, Kim JH, Chung JJ, Park MS, Lim JS, Oh YT. Focal hepatic lesions: detection and characterization with combination gadolinium- and superparamagnetic iron oxide-enhanced MR imaging. Radiology 2003;228:719–726.